

Physical Properties of H II Regions in M51 from Spectroscopic Observations

PENG WEI,^{1,2,3,4} HU ZOU,^{3,4} XU KONG,⁵ XU ZHOU,^{3,4} NING HU,^{5,6} ZESUN LIN,^{5,6} YEWELI MAO,⁷ LIN LIN,⁸ ZHIMIN ZHOU,³
XIANG LIU,¹ SHUGUO MA,^{1,2} LU MA,¹ TUHONG ZHONG,¹ FEI DANG,¹ JIANTAO SUN,¹ AND XINKUI LIN¹

¹*Xinjiang Astronomical Observatory, Chinese Academy of Sciences, Urumqi 830011, China*

²*School of Astronomy and Space Science, University of Chinese Academy of Sciences, Beijing 101408, China*

³*CAS Key Laboratory of Optical Astronomy, National Astronomical Observatories, Chinese Academy of Sciences, Beijing 100101, China*

⁴*Center for Astronomical Mega-Science, Chinese Academy of Sciences, 20A Datun Road, Chaoyang District, Beijing, 100012, P. R. China*

⁵*Key Laboratory for Research in Galaxies and Cosmology, Department of Astronomy, University of Science and Technology of China, Hefei 230026, China*

⁶*School of Astronomy and Space Science, University of Science and Technology of China, Hefei 230026, China*

⁷*Center for Astrophysics, GuangZhou University, GuangZhou 510006, P. R. China*

⁸*Shanghai Astronomical Observatory, Chinese Academy of Sciences, Shanghai 200030, China*

(Received; Revised; Accepted)

Submitted to

ABSTRACT

M51 and NGC 5195 is an interacting system that can be explored in great details with ground-based telescopes. The H II regions in M51 were observed using the 2.16 m telescope of the National Astronomical Observatories of the Chinese Academy of Sciences and the 6.5 m Multiple Mirror Telescope with spatial resolution of less than ~ 100 pc. We obtain a total of 113 spectra across the galaxy and combine the literature data of Croxall et al. to derive a series of physical properties, including the gas-phase extinction, stellar population age, star formation rate (SFR) surface density, and oxygen abundance. The spatial distributions and radial profiles of these properties are investigated in order to study the characteristics of M51 and the clues to the formation and evolution of this galaxy. M51 presents a mild radial extinction gradient. The lower gas-phase extinction in the north spiral arms compared to the south arms are possibly caused by the past encounters with the companion galaxy of NGC 5195. A number of H II regions have the stellar age between 50 and 500 Myr, consistent with the recent interaction history by simulations in the literatures. The SFR surface density presents a mild radial gradient, which is ubiquitous in spiral galaxies. There is a negative metallicity gradient of -0.08 dex R_e^{-1} in the disk region, which is also commonly found in many spiral galaxies. It is supported by the “inside-out” scenario of galaxy formation. We find a positive abundance gradient of 0.26 dex R_e^{-1} in the inner region. There are possible reasons causing the positive gradient, including the freezing of the chemical enrichment due to the star-forming quenching in the bulge and the gas infall and dilution due to the pseudobulge growth and/or galactic interaction.

Keywords: galaxies: abundances – galaxies: evolution – galaxies: individual (M51) – galaxies: ISM – galaxies: stellar content

1. INTRODUCTION

Understanding galaxy formation and evolution is one of the ultimate challenges in extragalactic astronomy.

Detailed investigations of the spatial distributions of stars, dust, and gas in galaxies can provide important information of galaxy formation and evolution, such as star formation, chemical enrichment, and mass assembly. Nearby galaxies provide one of the best laboratories for understanding the current star formation process and can be used to constrain the chemical evolu-

tion theories of galaxies (Osterbrock, & Ferland 2006; Dobbs et al. 2010).

Due to strong star formation and ionized hydrogen formed by high-energy radiation from young massive stars, H II regions are perfect probes for studying the star formation processes, evolution of young massive stars, and surrounding interstellar medium. Combining the spectroscopic and multi-wavelength photometric data, we can obtain a series of physical properties from the measurements of the nebular emission lines and underlying stellar continua, such as star formation rate (SFR; López-Sánchez 2010; Zhou et al. 2014; González Delgado et al. 2016), mass and luminosity (Rosales-Ortega et al. 2012; García-Benito et al. 2019), effective yield and rotation velocity (Pilyugin et al. 2004; Zou 2011a; Hu et al. 2018), stellar-to-gas fraction (Zahid et al. 2014), spatial distribution of gas-phase or stellar metallicity (Bresolin et al. 2004; Zou et al. 2011b,c; Lin et al. 2013; Sánchez et al. 2014; Pilyugin et al. 2014; Croxall et al. 2015; Ho et al. 2015; Lin et al. 2017; Hu et al. 2018), and stellar population parameters (Zou et al. 2011b; Sánchez-Blázquez et al. 2014a; Zhou et al. 2014; Hu et al. 2018).

In the past decades, the integral field spectrograph (IFS) plays an important role in understanding the nature of galactic structure, formation, and evolution. A number of IFS surveys have been carried out, e.g., SAURON (Bacon et al. 2001), CALIFA (Sánchez et al. 2012a), SAMI (Bryant et al. 2015), AMUSING (Galbany et al. 2016), and MaNGA (Bundy et al. 2015). Spatially-resolved spectroscopic data of galaxies in the local universe make it possible to statistically study the physical properties and their correlations in sub-galactic scale, such as the radial metallicity gradients (Sánchez et al. 2014; Pilyugin et al. 2014; Ho et al. 2015; Croxall et al. 2016; Sánchez-Menguiano et al. 2019), radial age gradients (Sánchez-Blázquez et al. 2014a), the relation between the abundance gradient and morphology, mass, or bar (Sánchez-Menguiano et al. 2018; Zinchenko et al. 2019), SFR as a function of Hubble type and of galaxy mass (González Delgado et al. 2016; Cano-Díaz et al. 2019), and global and local mass-metallicity relation (Tremonti et al. 2004; Rosales-Ortega et al. 2012; Barrera-Ballesteros et al. 2016).

Most IFS surveys focus on the galaxies with relatively small apparent sizes, generating the spatial resolutions of order of kpc or sub-kpc. Considering that nearby large galaxies are rather close to us and their sizes are too big to be covered by IFS observations due to relatively small field of view, we have undertaken a project of spectroscopic observations of H II regions in 20 nearby face-on spiral galaxies (Kong et al. 2014), us-

ing the long-slit spectrograph of the 2.16 m telescope (Fan et al. 2016) mounted at XingLong station of National Astronomical Observatories of China (NAOC) and multifiber spectrograph of the Multiple Mirror Telescope (MMT; Fabricant et al. 2005). With these samples, we can obtain high spatial-resolution (< 160 pc) spectroscopic data of galaxies to analyze the distributions of the galaxy observables in great details, including dust extinction, metal abundance, star formation, and stellar population. So far, we have obtained the largest spectral sample of H II regions for M33 and analyzed the spatial distribution of electron temperature and oxygen abundance (Lin et al. 2017). Hu et al. (2018) used 188 spectrum of H II regions of M101 to investigate the two-dimensional distributions of stellar population and kinematic properties of this galaxy.

As one of the 20 nearby galaxy samples, M51 has been observed by using both the long-slit of the 2.16 m telescope and multifiber spectrograph of the MMT. M51 (NGC 5194, also known as the Whirlpool nebula, $\alpha = 13^h 29^m 52.^s 711$, $\delta = +47^\circ 11' 42.'' 62$) is a grand-design face-on spiral galaxy with the Hubble type of Sbc. Since M51 and its peculiar companion galaxy NGC 5195 are a close interacting galaxy pair, substantial H II regions have been formed in its spiral arms. M51 presents the metal-rich feature and a shallow radial abundance gradient (Bresolin et al. 2004; Croxall et al. 2015). It was found that M51 and NGC 5195 underwent an interaction, which induced a burst of star formation about 340–500 Myr ago (Mentuch Cooper et al. 2012). Therefore, M51 is an excellent object for studying the current status of an interacting system. In this paper, we present the spectroscopic observations of the H II regions and derive a series of physical properties, including the extinction, SFR surface density, stellar age, and gas-phase metallicity, and study their spatial distributions. Through the properties and their spatial distributions, we try to obtain the characteristics of this galaxy and investigate evolutionary clues and possible influence of the galactic interaction. Table 1 lists some basic parameters for M51 and NGC 5195, which are adopted for analyzing the radial profiles in this paper.

The paper is structured as follows. Section 2 introduces the spectroscopic observations and corresponding data reduction. Section 3 describes the detailed measurements of different physical properties. Sections 4 shows the spatial distributions of these physical properties and presents related comparison and analysis. The summary is given in Section 5.

2. OBSERVATIONS AND DATA REDUCTION

2.1. Facilities and Observations

Table 1. Basic parameters for M51 and NGC 5195.

	Parameters	Parameter value	Reference ^a
M51	R.A. (J2000)	13 ^h 29 ^m 52. ^s 711	(1)
	Decl. (J2000)	+47°11′42.″62	(1)
	Distance	7.9 Mpc	(1)
	Inclination	22°	(2)
	P.A.	172°	(3)
	R_{25}	336.″6	(4)
NGC 5195	R_e	125.″1	(4)
	R.A. (J2000)	13 ^h 29 ^m 59. ^s 590	(1)
	Decl. (J2000)	+47°15′58.″10	(1)
	Distance	7.9 Mpc	(1)
	inclination	43°	(5)
	P.A.	91°	(5)

^aReferences: (1) NASA/IPAC Extragalactic Database (NED); (2) Colombo et al. (2014); (3) Walter et al. (2008); (4) Third Reference Catalog of Bright Galaxies (RC3) (de Vaucouleurs et al. 1995); (5) Spillar et al. (1992).

The H II regions were selected from the continuum-subtracted H α image from NASA/IPAC Extragalactic Database. The sources are detected in this H α image by SExtractor (Bertin & Arnouts 1996). The spectroscopic targets of H II regions are selected as those sources with at least 25 pixels (about 75 pc in radius) whose H α flux is larger than a critical value. Possible contaminations by foreground bright stars selected from Two Micron All Sky Survey Point Source Catalog (Skrutskie et al. 2006) were eliminated. The optical spectra of M51 were taken by the Optomechanics Research Inc.(OMR) long-slit spectrograph of the 2.16 m telescope (Fan et al. 2016) at the Xinglong Station of NAOC and the Hectospec multi-fiber positioner and spectrograph of the 6.5 m MMT telescope (Fabricant et al. 2005). The OMR spectrograph is deployed at the Cassegrain focus. It provides a dispersion of 4.8 Å pixel⁻¹ and a resolution of about 10 Å. The wavelength coverage is about 3600–8000 Å. The Hectospec is a moderate-resolution, multi-object optical spectrograph at the Cassegrain focus of the 6.5 m MMT telescope. The Hectospec fiber positioners allow the users to reconfigure 300 fibers to targets over the 1° focal surface in 300 seconds. Each fiber has a diameter of 1.″5, corresponding to about 57 pc at the distance of M51. The Hectospec 270 gpm grating with blaze wavelength at 5200 Å was used. The spectral coverage ranges from 3650 to 9200 Å. The dispersion is 1.21 Å pixel⁻¹ and the resolution is ~ 5 Å.

The M51 observations with the OMR spectrograph of the NAOC 2.16 m telescope started in 2008 March 9 and ended in 2014 March 23. A total of 19 nights were used. Bias and dome flat frames were taken at the beginning and end of every night. The He–Ar arc lamp was used for wavelength calibrations. Normally, we took two exposures for each object and each was about 1800 s. The left panel of Figure 1 presents the slit positions on the sky. The length of the spectrographic slit was about 4′ and the width was about 2.″5, corresponding to about 96 pc at the distance of M51. A total of 30 slit positions were selected. Some of them were placed along the major-axis and minor-axis directions of M51 and NGC 5195, which was aimed to obtain high signal-to-noise ratio (S/N) continua of the bulges. For other slits, we manually placed them to cover as many H II regions as possible. The sky spectra with exposure time of 1200 s were taken between two exposures of each slit position. Proper flux standard stars were selected from the catalog of International Reference Stars (IRS; Corbin et al. 1991). Their slit spectra were used for the flux calibration.

We were awarded half a night on 2012 February 10 by the Telescope Access Program (TAP¹) to use the multifiber spectrograph of the MMT telescope. The H II regions of M101 were preferentially targeted due to its larger size. M51 was considered as a secondary target to supplement the long-slit observations. It was unfortunate that the weather got worse after the M101 observation. Only a few spectra with good quality were obtained. The exposure time was 3600 s. The observations were taken at airmass of about 1.06 and the seeing was about 0.″8. The right panel of Figure 1 shows the fiber positions.

2.2. Spectral Data Reduction

The raw data taken by the NAOC 2.16 m telescope observations are processed using the IRAF software². We perform the bias subtraction, flat-field correction, cosmic-ray removal, and the sky-background subtraction. The spectrum of each H II region is extracted based on the dispersion trace of the flux standard star and then wavelength-calibrated by using the extracted spectrum of the He–Ar lamp at the same CCD position. Flux calibration is performed based on the observation of the flux standard star and the mean atmospheric extinction coefficients at the Xinglong Station.

¹ <http://info.bao.ac.cn/tap/>

² <http://iraf.noao.edu/iraf/web/iraf-homepage.html>

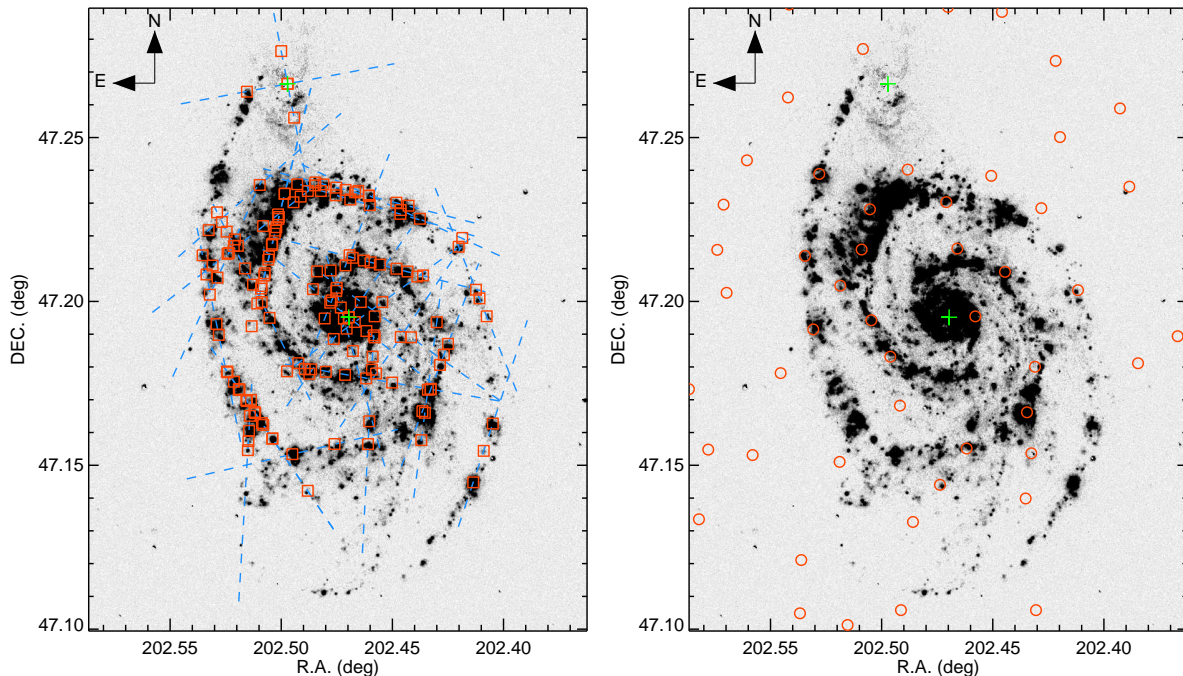


Figure 1. Left: slit positions (blue dashed line) placed on M51 observed by the NAOC 2.16 m telescope. The background gray-scale map is the continuum-subtracted $H\alpha$ narrowband image taken from NED. Green pluses imply the centers of M51 and NGC 5195. North is up and east is left. The red squares show the positions of the extracted spectra. Right: fiber positions (open circles) of the Hectospec multi-fiber positioner on the 6.5 m MMT telescope.

The MMT data are reduced with the publicly available HSRED v2.0 software³. After bias subtraction and flat-field correction, the fiber spectra are extracted and wavelength calibrated. The background sky emission is estimated by taking the average spectra with “blank sky” fibers in the same exposure and is subtracted from the individual spectrum. There is no observation for the flux standard star. The spectral energy distributions (SEDs) from the 15 intermediate-band photometric images of the Beijing–Arizona–Taipei–Connecticut (BATC) Color Survey of the Sky are utilized to calibrate the spectra (Lin et al. 2017).

There is a total of 250 extracted spectra, 113 of which are visually checked to have either good stellar continua or emission lines. Among the 113 spectra, 99 spectra are from the slits and the others are from the fibers. The furthest location of the spectra was ~ 10.5 kpc in terms of galactocentric distance of M51. All these spectra are resampled (keeping energy conservation) with a wavelength step of 1 \AA in the range of $3700\text{--}7500 \text{ \AA}$ using IRAF’s *dispcor* procedure. The 1 \AA step is selected according to the suggestion of STARLIGHT⁴ spectral

synthesis code (Cid Fernandes et al. 2005), as we want to get the stellar population age. These spectra are corrected for the Galactic extinction using the extinction law of Cardelli et al. (1989) and the reddening value of $E(B - V) = 0.031$ from the Galactic dust map of Schlegel et al. (1998).

3. SPECTRAL MEASUREMENTS

3.1. Full spectrum fitting and stellar age measurement

The underlying stellar continuum of each spectrum is modeled with the STARLIGHT spectral synthesis code. A grid of 150 simple stellar population (SSP) templates from Bruzual & Charlot (2003)⁵ with the Chabrier (2003) initial mass function (IMF) are used. These SSP templates cover 25 different ages (1 Myr–18 Gyr) and six metallicities ($0.005 - 2.5 Z_{\odot}$). The extinction law of Cardelli et al. (1989) is adopted to add dust extinction to the models. The observed spectrum is considered as a linear combination of the SSP templates. During the fitting of STARLIGHT, the wavelength regions covered by nebular emission lines and atmospheric absorption lines are masked. Figure 2 gives an example of the spectral fitting for two H II regions observed by

³ <http://mmto.org/rcool/hsred/index.html>

⁴ <http://www.starlight.ufsc.br>

⁵ <http://www.bruzual.org>

the NAOC 2.16 telescope and MMT. The best-fit model spectra are also overlapped in this figure.

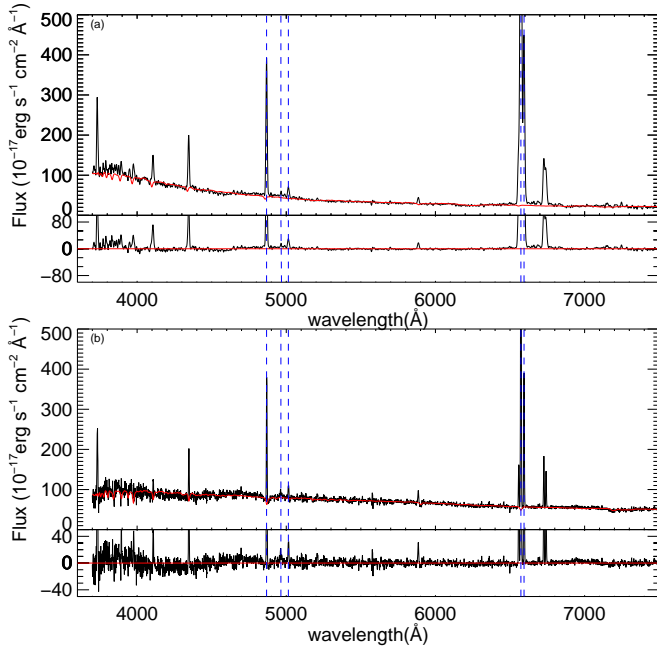


Figure 2. Upper: a high S/N observed spectrum of an H II region (black in the upper panel) observed by the NAOC 2.16 telescope. The best-fit model spectrum is overlapped in red. The residual spectrum between the observed and model spectra is plotted in the lower panel. The horizontal red line denotes the zero residual. The vertical dashed lines mark the emission lines used in this work. From left to right, they are H β , [O III] λ 4959, [O III] λ 5007, H α , and [N II] λ 6583, respectively. Bottom: the same as an arbitrarily selected H II region observed by the MMT telescope.

For each spectrum, we derive a stellar population age, which is a light-weighted average of the SSP compositions. In order to get a relatively reliable age estimate, the continuum S/N at ~ 5500 Å is required to be higher than 10. A total of 86 spectra have the age measurements. The uncertainty in logarithmic stellar age estimated by Cid Fernandes et al. (2005) is about 0.08 dex for S/N > 10.

3.2. Emission-line measurements

After the subtraction of the stellar continuum as modeled in Section 3.1, the emission-line fluxes of H β , [O III] λ 5007, H α , and [N II] λ 6583, which are used in this paper, are measured through the Gaussian function fitting. Only a few spectra (e.g. the ones at the galactic cores as shown in Figure 2) have the detections of other emission lines, such as [O II] and [S II], so their flux measurements are not provided. Due to relatively

low spectral resolution and low S/N of the spectra, the flux ratio between [N II] λ 6583 and [N II] λ 6548 is tied to theoretical values of 0.348, respectively. The profiles of H α , [N II] λ 6548, and [N II] λ 6583 are fitted simultaneously. Following Hu et al. (2018), the flux uncertainty of each emission line is estimated with the standard deviation within a wavelength region of 200 Å in width at the central wavelength of the emission line and errors induced by the Gaussian fitting.

3.3. Extinction estimation

The gas-phase extinction can be estimated with the Balmer line ratios, such as H α /H β , H α /H γ , and H β /H γ . The extinction estimation based on the Balmer lines is regarded to be independent on the physical conditions of the gas, such as the volume density and temperature (Domínguez et al. 2013). The H α and H β lines are detected in most of our spectra, so we use H α /H β to estimate the dust extinction.

Based on the assumptions of the reddening law of Cardelli et al. (1989), $R_V = 3.1$, and the intrinsic H α /H β of 2.86 under the Case B recombination of $T_e = 10,000$ K and $n_e = 100$ cm $^{-3}$ (Osterbrock, & Ferland 2006), the reddening value of $E(B-V)$ can be calculated as

$$E(B-V) = \frac{2.5}{k(\text{H}\beta) - k(\text{H}\alpha)} \log \frac{(\text{H}\alpha/\text{H}\beta)_{\text{obs}}}{(\text{H}\alpha/\text{H}\beta)_{\text{int}}}, \quad (1)$$

where $k(\text{H}\alpha)$ and $k(\text{H}\beta)$ represent the values of the reddening law at the wavelengths of the H α and H β lines, respectively. $(\text{H}\alpha/\text{H}\beta)_{\text{obs}}$ and $(\text{H}\alpha/\text{H}\beta)_{\text{int}}$ are the observed and intrinsic flux ratios, respectively. As described in Catalán-Torrecilla et al. (2015), the extinction curves and dust-to-stars geometries would have little effect on the attenuation calculation. We also check the effect of adding the dust curve of stellar content in the SSP fitting on the gas-phase extinction and find that it makes the gas-phase extinction difference within about 0.03 mag, which is quite smaller than the average measurement error of about 0.1 mag. In this paper, if the observed $\text{H}\alpha/\text{H}\beta \leq 2.86$, $E(B-V)$ is set to zero. All the fluxes of the emission lines used in this paper are corrected for this gas-phase extinction.

3.4. Σ_{SFR}

The SFR surface density is calculated as $\Sigma_{\text{SFR}} = \text{SFR}/\text{area}$. The area for a long-slit spectrum is calculated as the one of a rectangle, whose length is the aperture size used for extracting the spectrum and width is the slit width. The area for a fiber spectrum is calculated as the one of a circular, whose diameter is the fiber size. The SFR in $M_{\odot} \text{ yr}^{-1}$ is estimated with the

extinction-corrected $H\alpha$ luminosity ($L(H\alpha)$) by using the relation from Kennicutt (1998):

$$\text{SFR} = 7.9 \times 10^{-42} L(H\alpha) (\text{erg s}^{-1}). \quad (2)$$

This SFR calculator is derived based on the Salpeter IMF with stellar masses in the range of $0.1\text{--}100 M_{\odot}$. Note that the $H\alpha$ luminosity is calibrated by using the aperture flux of $3''$ in diameter in the Sloan Digital Sky Surveys r -band image.

3.5. Metallicity Determination

The so-called *direct* T_e method is the most reliable way to measure gas-phase oxygen abundance, which is based on the ratio of auroral line intensities, such as $[\text{O III}]\lambda 4363/\lambda 5007$ (Osterbrock, & Ferland 2006). However, it is difficult to detect these auroral lines in our spectra, which are $\sim 100\text{--}1000$ times fainter than $H\beta$. There are multiple strong-line methods to estimate the gas-phase oxygen abundance of galaxies, including R23 (Kobulnicky et al. 1999; Pilyugin, & Thuan 2005), N2 (Pettini, & Pagel 2004; Marino et al. 2013), O3N2 (Pettini, & Pagel 2004; Marino et al. 2013), N2O2 (Kewley & Dopita 2002; Bresolin 2007), etc. Since only a few spectra have the detection of $[\text{O II}]\lambda 3727$, those metallicity estimators related to this line is not applicable. Although $[\text{N II}]\lambda 6583$ and $H\alpha$ lines are detected for most of our spectra, the metallicity based on the N2 index ($\text{N2} \equiv \log([\text{N II}]\lambda 6583/H\alpha)$) reaches saturation in the solar and super-solar metallicity regime with the N2 calibration (Pettini, & Pagel 2004). Thus, we use the O3N2 index to estimate the gas-phase oxygen abundance, where

$$\text{O3N2} = \log\left(\frac{[\text{O III}]\lambda 5007/H\beta}{[\text{N II}]\lambda 6583/H\alpha}\right). \quad (3)$$

We adopt the O3N2 metallicity calibration of Marino et al. (2013), which is expressed as

$$12 + \log(\text{O}/\text{H}) = 8.533 - 0.214 \times \text{O3N2}. \quad (4)$$

This calibration is valid in the range of $-1.1 < \text{O3N2} < 1.7$ and the calibration uncertainty is about 0.18 dex (Marino et al. 2013). The random error of the metallicity, which is provided in the rest of this paper, comes from the emission-line measurements.

4. RESULTS

Table 2 in the Appendix A shows all the emission line measurements and corresponding spectral properties. A total of 113 spectra with $H\alpha$ and $H\beta$ flux S/N greater than 5 are presented. All the emission-line fluxes are corrected for the gas-phase extinction. The $H\beta$ flux is

the absolute line strength, while other line fluxes are relative ones, which are normalized to the $H\beta$ flux. The metallicity measurement requires that $[\text{O III}]\lambda 5007$ and $[\text{N II}]\lambda 6583$ have S/Ns higher than 5 (a total of 67 regions). The age measurement requires that the continuum S/N at 5500 \AA higher than 10 (a total of 86 regions).

In order to discriminate dominant ionizing sources, we apply the Baldwin–Phillips–Terlevich (BPT) diagram and the equivalent width of $H\alpha$ ($\text{EW}(H\alpha)$) to examine the excitation properties of the spectra. As shown in Figure 3, the BPT diagram presents the $[\text{O III}]\lambda 5007/H\beta$ line ratio against $[\text{N II}]\lambda 6583/H\alpha$ (Baldwin et al. 1981). Two lines from Kewley et al. (2001) and Kauffmann et al. (2003) are adopted to separate pure star-forming, active galactic nuclei (AGNs), and composite regions. As described in Lacerda et al. (2018), the $\text{EW}(H\alpha)$ can be also used to diagnose different ionization sources in a single galaxy: regions where $\text{EW}(H\alpha) < 3 \text{ \AA}$ are ionized by hot low-mass evolved stars, regions where $\text{EW}(H\alpha) > 14 \text{ \AA}$ are related to the ionization due to young OB stars in H II regions and trace the star formation complexes, and regions where $3 \text{ \AA} < \text{EW}(H\alpha) < 14 \text{ \AA}$ are contributed by more than one process. The $\text{EW}(H\alpha)$ of our spectra is shown as the colors of the data points in Figure 3.

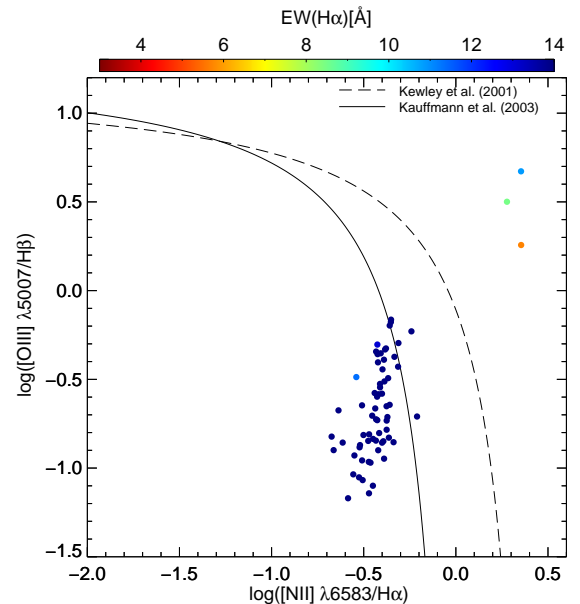


Figure 3. Our spectral samples on the BPT diagram presenting the $[\text{O III}]\lambda 5007/H\beta$ line ratio against $[\text{N II}]\lambda 6583/H\alpha$. The curves with solid and dashed lines are from Kauffmann et al. (2003) and Kewley et al. (2001), respectively. The color of each point indicates the equivalent width of $H\alpha$ of each spectra.

In the BPT diagram, the data points above the Kewley et al. (2001) curve are regarded as the regions possibly affected by AGN. Three points are located in the AGN region and the $\text{EW}(\text{H}\alpha)$ is smaller than 14 \AA . These points are closed to the nucleus of M51, which has the AGN activity as reported by Goad et al. (1979) and Moustakas et al. (2010). These exceptions, which is specially noted in Table 2, are excluded in the following analyses. There are additional 2 points with $\text{EW}(\text{H}\alpha) < 14 \text{ \AA}$. Most of our samples are star-forming regions close to or below the Kauffmann et al. (2003) curve and their $\text{EW}(\text{H}\alpha)$ is larger than 14 \AA . All other spectra that have not enough S/Ns of emission lines and thus are not on the BPT diagram are located far away from the M51 nucleus, and their $\text{EW}(\text{H}\alpha)$ is larger than 14 \AA . It is believed that our spectra mainly come from star-forming regions.

4.1. Extinction distribution

Based on the Balmer decrement and assumed reddening law of Cardelli et al. (1989), we derive the extinction in A_V and map the extinction distribution in Figure 4. In this figure, we also present the extinctions derived by Croxall et al. (2015), who obtained the spectra of 59 H II regions in M51 from the CHemical Abundances Of Spirals (CHAOS) project (Berg et al. 2015). In the paper of Croxall et al. (2015), the extinction was given at $\text{H}\beta$. The $\text{H}\beta$ extinction $c(\text{H}\beta)$ is converted to A_V following $c(\text{H}\beta) = 1.43E(B - V)$ and $A_V = 3.1E(B - V)$ (Berg et al. 2015). The overall average gas-phase extinction is about 1.18 mag. The core region of M51 presents a larger gas-phase extinction than the outside.

The radial extinction distribution is shown in Figure 5a. We can see that there is a mild extinction gradient, although the radial extinction presents a relatively large dispersion. From the extinction map in Figure 4, we can also see that the extinction in the northern spiral arms is generally smaller than the southern ones. Therefore, we try to divide the spectral samples into north and south regions and present their radial extinction distributions in Figure 5b and 5c, respectively. The line of the minor axis of M51 is considered as the boundary, which is plotted in dashed line in Figure 4. From these radial distributions, we find that the dispersions get reduced compared to the whole distribution and the gas-phase extinction of the north region, which is close to NGC 5195, is generally smaller than that of the south one. The M51–NGC 5195 system has undergone more than once close encounters and the last one possibly occurred 300–500 Myr ago, which was inferred from kinematic and hydrodynamic simulations (Salo & Laurikainen 2000; Dobbs et al. 2010).

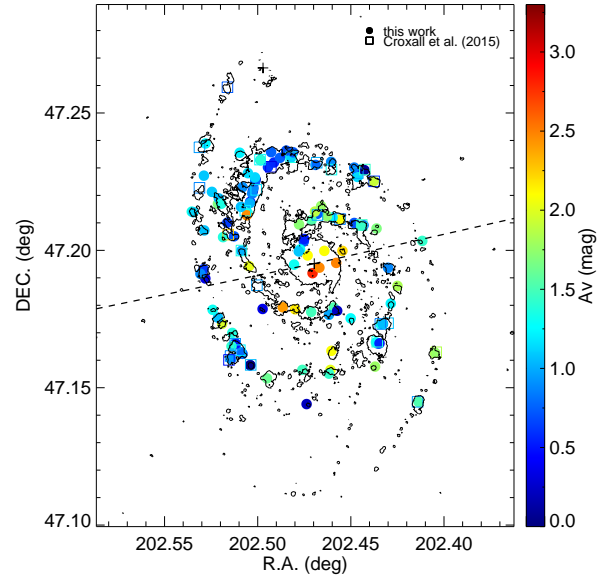


Figure 4. Two-dimensional distribution of the gas-phase extinction A_V across M51. The contours display the isophotal shapes of the $\text{H}\alpha$ emission. The centers of M51 and NGC 5195 are marked with pluses. The filled-circles are the extinctions obtained in this work and the open-squares are the extinctions from Croxall et al. (2015). The dashed line shows the direction of the minor axis, which is used as the boundary between the northern and southern parts of M51.

The close encounter might disperse the gas distribution in the north parts more seriously and lead to the low gas-phase extinction, although more observational evidence is needed.

4.2. Stellar age and Σ_{SFR} distributions

The left panel of Figure 6 shows the distribution of the stellar age. The middle panel of Figure 6 shows the spatial distribution of the equivalent width of the $\text{H}\alpha$ line ($\text{EW}(\text{H}\alpha)$). The $\text{EW}(\text{H}\alpha)$ is sensitive to the ratio of present to past SFRs (see Kong et al. 2004, and references therein) and is related to the strength of ionization of the ionization source (Lacerda et al. 2018; Sánchez 2020). We have eliminated the regions influenced by AGN. The $\text{EW}(\text{H}\alpha)$ of the majority of our samples are larger than 14 \AA , so they are related to the ionization due to young stellar population. The maps of the stellar age and $\text{EW}(\text{H}\alpha)$ are generally consistent as shown in Figure 6. The bulge of M51 is older than the outskirt and the inner arms are older than the outer arms. This kind of decreasing radial age profile supports the “inside-out” galaxy growth scenario, which is suitable for a majority of disk galaxies (Sánchez-Blázquez et al. 2014a; Sánchez 2020). There are considerable H II regions in the outer arms with age of 50 – 500 Myr. The recent close encounter between M51 and NGC 5195 can

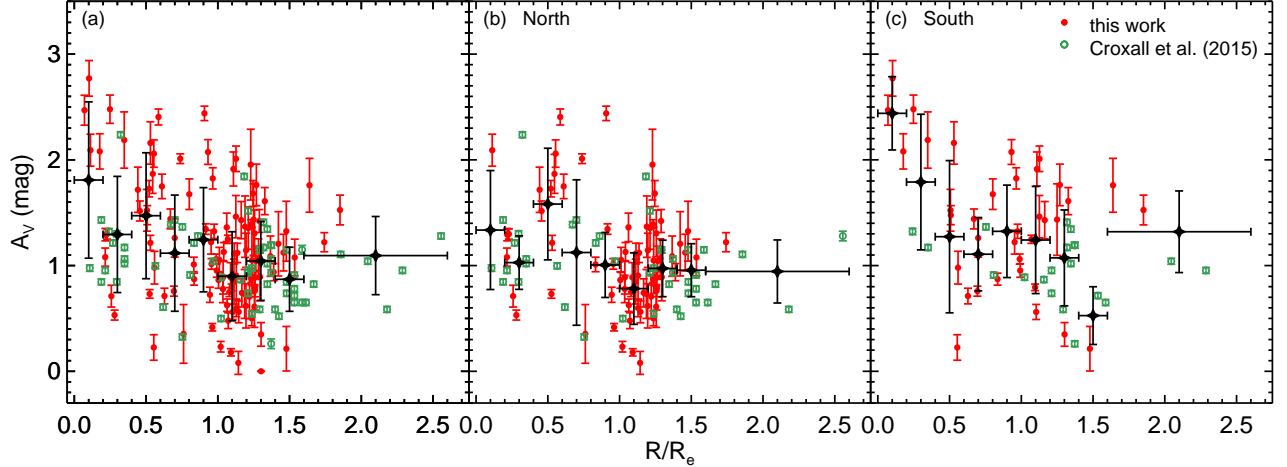


Figure 5. (a) Deprojected radial extinction distribution of all our H II-region samples in M51. Here R_e is the effective radius of M51, which is shown in Table 1. The filled-circles and open-circles are the data from this work and Croxall et al. (2015), respectively. The black star with vertical error bar presents the average extinction and its standard deviation in each radial bin, while the horizontal bar shows the range of each bin. (b) Deprojected radial extinction distributions of the north part. (c) Deprojected radial extinction distributions of the south part.

trigger substantial star formation and form young stellar populations. We also obtain the light-weighted mean stellar age of three regions in NGC 5195, including one in the galactic core and two in the disk. All of them are very old stellar population and the average age is about 10 Gyr. Almost no recent star formation is found in this galaxy, since there is lack of any $H\alpha$ radiation.

Calzetti et al. (2005) reported that M51 is a typical star-forming galaxy with the total SFR $\sim 3.4 M_\odot \text{ yr}^{-1}$ and $\Sigma_{\text{SFR}} = 0.015 M_\odot \text{ yr}^{-1} \text{ kpc}^{-2}$. The right panel of Figure 6 shows Σ_{SFR} distribution of the H II regions in M51. We can also see that there is on-going star formation in the bulge region of M51. There is no obvious difference of Σ_{SFR} between the northern and southern spiral arms. Although the close encounters can trigger star formation through the perturbation, they might disperse the gas more widely in the north, such that the north part presents similar Σ_{SFR} to the south. It can be also seen from the $H\alpha$ map that the $H\alpha$ emission looks more diffuse in the northern arms. Nevertheless, we need more observational evidence to support it.

In Figure 7, we present the radial distribution of Σ_{SFR} . From this figure, we can see there is a monotonic decrease of the radial Σ_{SFR} in M51, although the radial profile presents a relatively large dispersion. The gradient is about $-0.55 \text{ dex } R_e^{-1}$. González Delgado et al. (2016) characterized the radial structure of Σ_{SFR} of the CALIFA galaxies, and they found that Σ_{SFR} of all spiral galaxies decreases with radial distance. The typical gradient in the central $1 \times R_e$ is about $-0.78 \text{ dex}/R_e$. Sánchez (2020) presented the radial distributions of Σ_{SFR} for low-redshift galaxies of different stellar

mass and morphology based on the recent IFS surveys. M51 is a Sbc-type galaxy and its stellar mass is about $4.7 \times 10^{10} M_\odot$ (Mentuch Cooper et al. 2012). We overlay the radial Σ_{SFR} profile from Sánchez (2020) for galaxies with the same morphological type and similar stellar mass in Figure 7. It shows that the radial Σ_{SFR} gradient of M51 is similar to the galaxies of similar mass and morphology in the nearby universe.

4.3. Chemical Abundance Distribution

4.3.1. The Spatial Distribution of Oxygen Abundances

There are a total of 67 H II regions in M51 whose gas-phase oxygen abundances are estimated using the O3N2 calibration. The two-dimensional distribution of the oxygen abundance is shown in the left panel of Figure 8. The data obtained by Croxall et al. (2015) are also overplotted in this figure. Although Croxall et al. (2015) derived the oxygen abundance through the direct T_e method, we recalculate the metallicity using the same O3N2 calibration as used in this paper. Note that different strong-line calibrators may give distinct absolute values of metallicity.

The right panel of Figure 8 shows the radial profile of the oxygen abundance. The data points from Croxall et al. (2015), recalculated by with the same O3N2 calibration, are also presented in this figure. These two datasets are complementary. It is interesting that there are two different gradients in the inner and outer regions. The inner region presents a positive gradient and the outer disk region shows a negative one. We perform two independent linear fits to the radial profile. The cutoff point is manually set at $R/R_e = 0.4$,

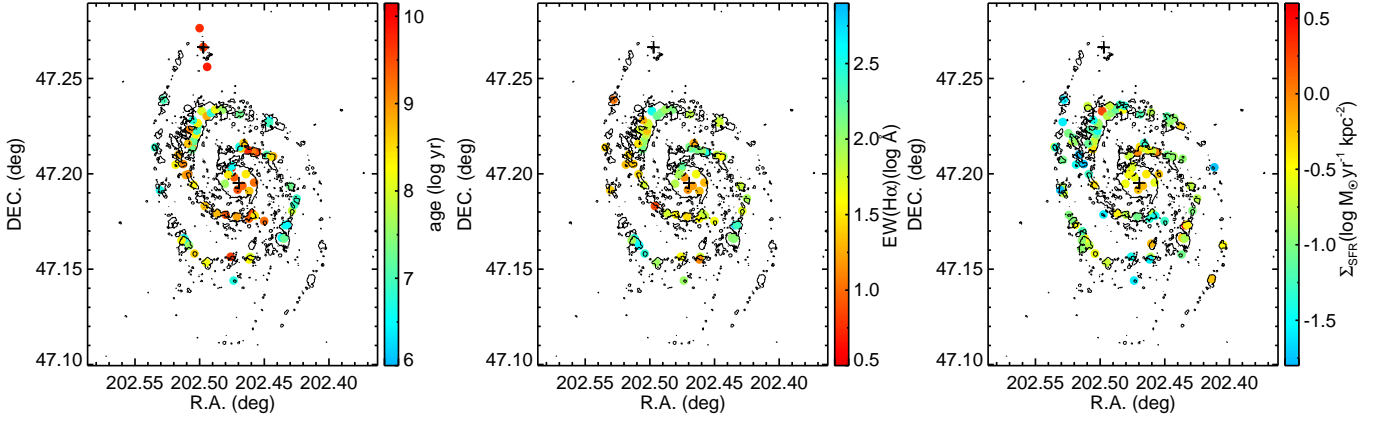


Figure 6. Left: spatial distribution of light-weighted mean stellar population age in logarithmic scale. Middle: spatial distribution of $EW(H\alpha)$. Right: spatial distribution of Σ_{SFR} in logarithmic scale. The contours display the isophotal shapes of the $H\alpha$ emission. The centers of M51 and NGC 5195 are marked with pluses.

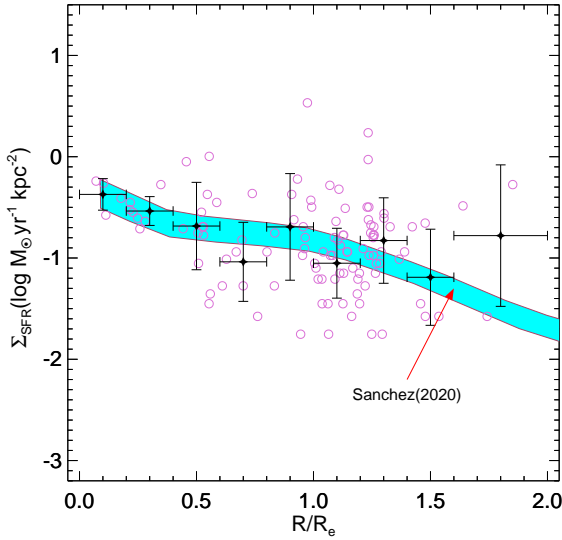


Figure 7. Deprojected radial distribution of Σ_{SFR} . The black star with error bar present the mean value and its standard deviation in each radial bin, while the horizontal bars show the range of each bin. The radial distribution of Σ_{SFR} for Sbc-type galaxies with $10^{10.5} M_{\odot} < M_{*} < 10^{11} M_{\odot}$ from Sánchez (2020) is shifted upward by 1.4 dex to match our data and overplotted in cyan.

which is around the turn point of the radial profile as seen in Figure 8. It is corresponding to the angular distance of about $50''$ and the galactocentric distance of 1.9 kpc. The region of $R/R_e < 0.4$ includes the bulge (size of $11'' \times 16''$, Lamers et al. 2002) and surrounding star

forming ring. The linear fits are expressed as

$$\begin{aligned} 12 + \log(O/H)[O3N2] \\ &= (8.70 \pm 0.02) - (0.08 \pm 0.015) \times R/R_e \\ &= (8.70 \pm 0.02) - (0.22 \pm 0.04) \times R/R_{25}, \end{aligned} \quad (5)$$

for $R/R_e > 0.4$ or $R/R_{25} > 0.15$, and

$$\begin{aligned} 12 + \log(O/H)[O3N2] \\ &= (8.53 \pm 0.02) + (0.26 \pm 0.09) \times R/R_e \\ &= (8.53 \pm 0.02) + (0.71 \pm 0.25) \times R/R_{25}, \end{aligned} \quad (6)$$

for $0 < R/R_e < 0.4$ or $0 < R/R_{25} < 0.15$. In Figure 8, we also present the linear fits with only our data and only the data of Croxall et al. (2015). The corresponding gradients in the outer region are -0.05 ± 0.025 and -0.10 ± 0.02 dex R_e^{-1} , respectively. These gradients are consistent with that of the combined data within the uncertainty. Combining two datasets should provide more reliable gradient measurements, because we use the same metallicity calibrator. The metallicity gradients as shown in Equation (5) and (6) are adopted in the following analyses.

4.3.2. Comparison with Previous Work

The radial negative gradient of the oxygen abundance in the disk region (-0.22 ± 0.04 dex R_{25}^{-1}) is close to other measurements based on different diagnostic methods. Moustakas et al. (2010) used the empirical R_{23} calibration of Pilyugin, & Thuan (2005) and provided an abundance gradient of about -0.31 ± 0.06 dex R_{25}^{-1} for about 20 H II regions. Bresolin et al. (2004) used a sample of 10 H II regions with the T_e measurements and obtained a gradient of -0.28 ± 0.14 dex R_{25}^{-1} . Croxall et al. (2015) derived an abundance gradient of -0.30 ± 0.10 dex R_{25}^{-1} .

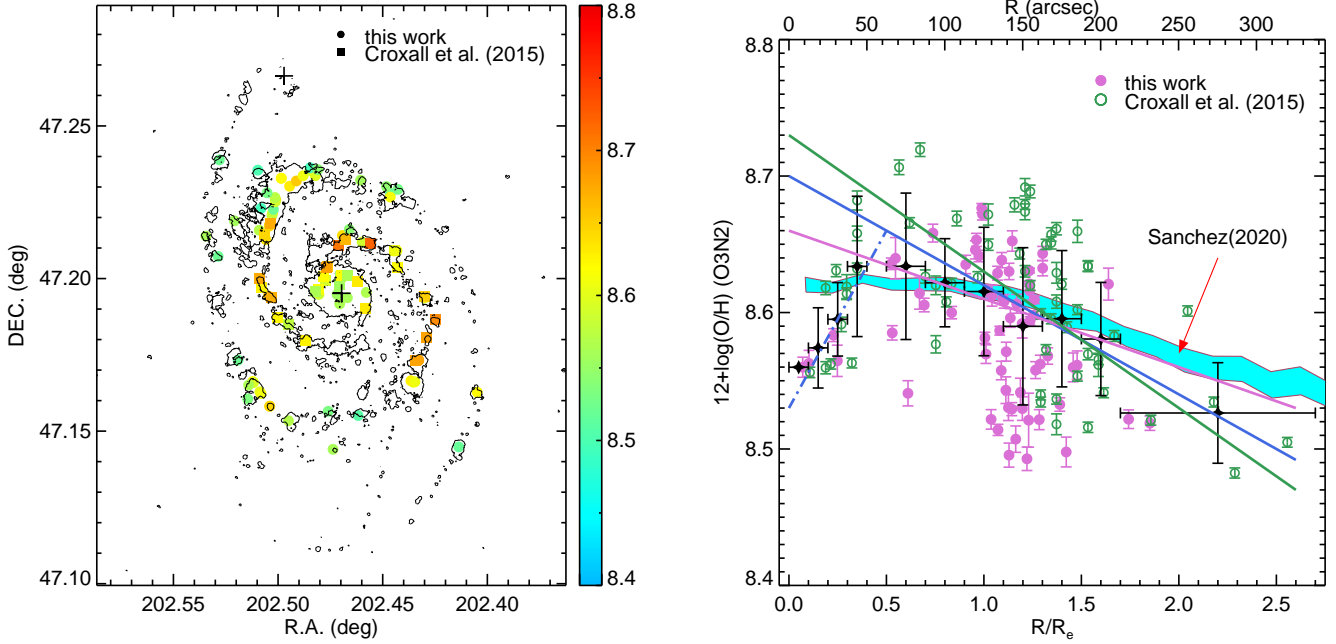


Figure 8. Left: two-dimensional distribution of the oxygen abundance of H II regions in M51. The contours display the isophotal shapes of the H α emission. The centers of M51 and NGC 5195 are marked with pluses. Right: radial distribution of the oxygen abundance. The filled circles and open circles are the data from this work and Croxall et al. (2015), respectively. The black stars with error bars are the mean values, while the horizontal bars show the range of each bin. The blue dashed line shows the positive slope at $R/R_e < 0.4$, while the blue solid line shows the negative gradient at $R/R_e > 0.4$. The violet and green lines display the gradients for the data in our work and the data of Croxall et al. (2015) at $R/R_e > 0.4$, respectively. The radial distribution of oxygen abundance for Sbc-type galaxies with $10^{10.5} M_\odot < M_* < 10^{11} M_\odot$ from Sánchez (2020) is shifted to match our data and overplotted in cyan.

through the temperature-sensitive auroral lines for 29 individual H II regions. Considering different calibration methods and limited H II samples, our estimate of the metallicity gradient for the M51 disk is in agreement with the above measurements within the uncertainties. Our abundance gradient is statistically more accurate, since we include a large number of H II regions.

It is well known that negative radial gradients of the gas-phase metallicity are ubiquitous in many disk galaxies (Searle 1971; Oey, & Kennicutt 1993; Zaritsky et al. 1994; Moustakas et al. 2010). It can be simulated by chemical evolution models, indicating an “inside-out” galaxy growth. The oxygen abundance gradient of the M51 disk ($-0.22 \pm 0.04 \text{ dex } R_{25}^{-1}$) is shallower than some other isolated spiral galaxies, such as NGC 628 ($-0.485 \pm 0.122 \text{ dex } R_{25}^{-1}$, Berg et al. 2015), NGC 2403 ($-0.524 \pm 0.043 \text{ dex } R_{25}^{-1}$, Pilyugin et al. 2014), and M101 ($-0.832 \pm 0.044 \text{ dex } R_{25}^{-1}$, Croxall et al. 2016). However, such a comparison is less persuasive due to a small sample. Kewley et al. (2010) and Sánchez et al. (2014) found evidence that the interacting systems present shallower metallicity gradients compared to the isolated galaxies. Recently, the IFS surveys have offered

the opportunity to achieve meaningful statistical results about abundance gradients for large samples of galaxies in the Local universe with different properties, such as morphology, stellar mass, and environment density (Sánchez et al. 2014; Ho et al. 2015; Belfiore et al. 2017; Sánchez-Menguiano et al. 2018; Sánchez 2020). Using the high spatial resolution IFS data obtained by MUSE, Sánchez-Menguiano et al. (2018) found that spiral galaxies present a characteristic abundance slope of $-0.10 \pm 0.03 \text{ dex}/R_e$ between $0.5 R_e$ and $1.5 R_e$. Our gradient measurement of the M51 disk is consistent with this characteristic slope. Sánchez-Menguiano et al. (2018) also studied the possible effect of the density of the galaxy environment on the metallicity gradient and claimed that their spiral galaxy samples present a similar slope independent of the environment. It is worthy to notice that they discarded those distorted galaxies with recent interactions (like the M51-NGC 5195 system) in their analysis. Sánchez (2020) showed the radial profiles of the oxygen abundance for galaxies of different morphology and stellar mass. From Figure 15 in Sánchez (2020), the typical gradient is about $-0.06 \text{ dex } R_e^{-1}$ for $10^{10.5} M_\odot < M_* < 10^{11} M_\odot$ and Sbc type in the range

of $0.4R_e < R < 2R_e$. We also present the radial metallicity profile from Sánchez (2020) in the Figure 8. It seems that the M51 disk does not present much difference of the metallicity gradient from those galaxies with similar stellar mass and morphological type within the measurement uncertainty. According to the above comparison with the literature, the interaction does not seem to have a significant impact in the metallicity gradient measured in the disk of M51.

From the right panel of Figure 8, we can see that a dozen H II regions at $R < 0.4R_e$ show systematically lower metallicities, compared to the extrapolated oxygen abundance of the outer disk into the inner region. There have been observational evidences based on IFU data that some galaxies present some different behaviors from a simple negative radial gradient in the innermost and outer parts (Sánchez et al. 2014; Sánchez-Menguiano et al. 2018; Sánchez 2020). These studies found that the oxygen abundance of galaxies sometimes presents a prominent flattening or drop in the inner regions. The inner drop is ubiquitous in massive galaxies with $M_* > 10^{10}M_\odot$ (Sánchez 2020, and references therein) and it always appears at a similar location of $R \sim 0.5R_e$ for all galaxies (Sánchez-Menguiano et al. 2018). M51 presents a drop at almost the same location. A possible cause to the inner drop as mentioned by Sánchez (2020) is the effect of radial migration to the Lindblad resonances or the freezing of the chemical enrichment due to the star-formation quenching in the bulge-dominated inner region. Sánchez et al. (2015) claimed that the ionization conditions of H II regions seem to be closely related to the properties of the underlying stellar population. It means that the metal enrichment of an H II region is not necessarily correlated with the most recent star formation but rather to the local star-formation history. Recent encounters in M51 may induce gas infall and form new H II regions in the inner region, but they might keep a memory of the local metal enrichment in the history, when the chemical enrichment could be frozen due to the star-formation quenching. Thus, the inner region of M51 might still keep the relative poor metallicity and cause a positive metallicity gradient.

On the other hand, we also notice that the bulge of M51 is a so-called pseudobulge (Fisher & Drory 2010), which presents a near-exponential surface brightness profile, rotating motion, active star formation, nuclear bar, ring and/or spiral (Kormendy & Kennicutt 2004). The non-axisymmetric nuclear bar and spiral arms can drive the gas infall, facilitate the pseudobulge growth, and cause higher gas-phase extinction and active star formation in the inner region of M51 as shown in Fig-

ure 4 and 6. A rather chaotic distribution of dust lanes can be found in high-resolution images of the central region of M51 taken by the Hubble Space Telescope, which also indicates that M51 is transporting gas to the nucleus (Grillmair et al. 1997). The gas inflow into the galactic center might dilute the metallicity and hence form a positive gradient. Another possible reason for the inner drop is the interaction between M51 and NGC 5195, which might also induce the gas inflow and the radial mixing.

5. SUMMARY

Nearby galaxies are ideal laboratories for understanding the galaxy formation and evolution in great details. M51 is undergoing the gravitational interaction with its companion of NGC 5195 at the distance of about 7.9 Mpc. It is an excellent object to investigate the spatial distributions of the physical properties and seek the possible clues of the formation and evolution for similar galaxies. There are substantial H II regions across the whole galaxy of M51. As one of 20 large nearby spiral galaxies in our observing program (Kong et al. 2014), a large number of H II regions of M51 have been observed by using the NAOC 2.16 m and 6.5 m MMT telescopes. A total of 113 spectra are obtained: 99 of them are from the long-slit spectrograph and the rest are the fiber spectra. Together with the literature data of Croxall et al. (2015), we derive the two-dimensional distributions and corresponding radial gradients of a series of physical properties and try to explore the possible evolution clues of this galaxy and the influence of the galactic interaction. Through the emission line measurements and spectral fitting, we obtain the gas-phase extinction, SFR surface density, stellar population age, oxygen abundance, and their corresponding spatial distributions. Some of the main points in this paper is summarized as follows:

- (1) There is a mild radial extinction gradient. The gas-phase extinction in the northern spiral arms that are close to NGC 5195 is lower than that of the southern arms. It might be related to the galactic interaction, which disperses the gas distribution in the area close to the companion.
- (2) M51 has a number of young H II regions with age of 50–500 Myr, which is consistent with the recent close interaction history with NGC 5195. Similar to most spiral galaxies, M51 presents a mildly radial gradient of the SFR surface density.
- (3) Three spectra for NGC 5195 are obtained in its bulge and disk. It is presented that NGC 5195 is an old

galaxy with average age of about 10 Gyr and no recent star formation occurs in this galaxy.

- (4) There is a radial negative gradient of gas-phase metallicity in the disk of M51 ($-0.08 \text{ dex } R_e^{-1}$). The age distribution and the radial negative gradient supports the “inside-out” galaxy growth. There is no clear evidence that the metallicity gradient is flattened by the galactic interaction.
- (5) There is a positive metallicity slope in the inner region, which include the bulge and surrounding star forming ring. This metallicity drop might be caused by the freezing of the chemical enrichment due to the star-forming quenching in the bulge-dominated inner region. Another possible reason is the growth of the pseudobulge and/or galactic interaction, which might induce the gas infall and dilute the metallicity in the center.

We thank the anonymous referee for his/her thoughtful comments and insightful suggestions that improve

our paper greatly. This work is supported by the Xinjiang Natural Science Foundation (No. 2020D01B59) and Major Program of National Natural Science Foundation of China (No. 11890691). This work is supported by the National Key R&D Program of China (973 Program; grant Nos. 2017YFA0402600), the National Natural Science Foundation of China (NSFC, grant Nos. 11673027, 11733007, 11973038, 11320101002, 11421303, 11890693), and the External Cooperation Program of Chinese Academy of Sciences (grant No. 114A11KYSB20160057). This work uses the observational time of the 2.16m telescope at the Xinglong station of the National Astronomical Observatories of China and the observational time of the MMT telescope obtained via the Telescope Access Program (TAP), which is funded by the National Astronomical Observatories of China, the Chinese Academy of Sciences (the Strategic Priority Research Program, “The Emergence of Cosmological Structures” grant No. XDB09000000), and the Special Fund for Astronomy from the Ministry of Finance. The 2.16m telescope is jointly operated and administrated by the National Astronomical Observatories of China and Center for Astronomical Mega-Science, Chinese Academy of Sciences.

APPENDIX

A. PHYSICAL PROPERTIES OF H II REGIONS IN M51

We present the physical properties derived from the observed spectra in this paper, which is shown in Table 2. This table contains the emission line measurements and corresponding derivatives. For more information, we can refer to Section 3.

Table 2. Emission-line Measurements and Spectral Properties

ID	R.A.	Decl.	R/R_{25}	[O III]	H α	[N II]	H β	EW(H α)	$E(B - V)$	12+log(O/H)	Σ_{SFR}	log (age)
(1)	(2)	(3)	(4)	(5)	(6)	(7)	(8)	(9)	(10)	(11)	(12)	(13)
1	13:30:1.318	47:12:49.427	0.341		2.942	1.087	1553.557	89.963	0.434		0.238	8.887
					0.017	0.008	24.614	0.513	0.016			
2	13:30:0.974	47:13:3.463	0.357	0.086	2.885	0.900	823.109	80.628	0.134	8.653	0.124	8.450
				0.004	0.008	0.004	9.541	0.217	0.011	0.005		
3	13:30:0.626	47:13:17.758	0.379	0.146	2.874	1.021	433.346	51.129	0.075	8.616	0.065	8.359
				0.006	0.016	0.009	6.993	0.278	0.016	0.004		
4	13:30:0.260	47:13:32.741	0.406	0.108	2.871	0.967	390.016	54.416	0.058	8.638	0.058	7.398
				0.006	0.007	0.004	4.418	0.129	0.011	0.006		
5	13:29:59.634	47:13:58.326	0.458	0.139	2.913	1.159	6142.437	253.225	0.282	8.631	0.933	7.110
				0.002	0.009	0.004	68.908	0.785	0.011	0.002		
6	13:30:1.403	47:12:45.939	0.337	0.126	3.010	1.141	2701.989	136.221	0.787	8.635	0.424	7.245
				0.009	0.023	0.009	58.961	1.056	0.022	0.007		
7	13:30:1.014	47:13:1.924	0.355	0.089	2.921	0.871	1335.628	98.341	0.327	8.646	0.204	7.205
				0.006	0.011	0.004	22.093	0.379	0.016	0.007		
8	13:30:0.707	47:13:14.408	0.374	0.217	2.912	1.063	603.281	61.893	0.278	8.582	0.092	8.330
				0.008	0.016	0.008	15.570	0.344	0.025	0.004		
9	13:30:0.531	47:13:21.535	0.385	0.472	2.914	1.217	245.681	22.338	0.287	8.522	0.037	6.913
				0.024	0.033	0.022	12.876	0.252	0.051	0.007		
10	13:30:0.311	47:13:30.654	0.402	0.197	2.905	1.021	687.594	62.071	0.242	8.587	0.104	6.976
				0.006	0.012	0.006	9.451	0.262	0.014	0.003		
11	13:29:59.634	47:13:58.326	0.458	0.143	2.944	1.084	11208.229	329.473	0.449	8.621	1.721	8.005
				0.002	0.019	0.007	141.557	2.130	0.014	0.002		
12	13:29:44.879	47:09:27.650	0.471		2.967	1.117	550.305	82.368	0.569		0.085	
					0.036	0.017	36.247	0.987	0.064			
13	13:29:44.491	47:09:57.670	0.407	0.131	2.908	0.873	1489.537	126.645	0.256	8.610	0.226	7.772
				0.002	0.007	0.003	14.316	0.308	0.010	0.002		
14	13:29:44.165	47:10:23.048	0.362	0.107	2.940	1.012	22199.240	671.499	0.427	8.641	3.405	6.871
				0.004	0.031	0.009	446.091	7.158	0.022	0.004		
15	13:29:43.206	47:11:37.137	0.310	0.154	2.913	0.918	1177.172	63.185	0.281	8.600	0.179	7.281
				0.007	0.010	0.005	22.354	0.211	0.018	0.005		
16	13:30:2.113	47:11:59.316	0.310		2.921	0.959	368.112	28.493	0.326		0.056	9.025
					0.013	0.008	8.436	0.130	0.022			
17	13:30:3.047	47:12:18.364	0.351		2.904	0.892	131.759	23.515	0.233		0.020	9.029
					0.013	0.008	3.151	0.103	0.023			
18	13:30:3.918	47:12:36.216	0.396		2.898	1.024	137.162	27.585	0.201		0.021	8.755
					0.011	0.007	2.692	0.109	0.019			
19	13:30:5.127	47:13:0.949	0.463		2.962	0.903	1366.686	140.693	0.543		0.211	

Table 2 continued

Table 2 (continued)

ID	R.A.	Decl.	R/R_{25}	[O III]	H α	[N II]	H β	EW(H α)	$E(B - V)$	12+log(O/H)	Σ_{SFR}	log (age)
(1)	(2)	(3)	(4)	(5)	(6)	(7)	(8)	(9)	(10)	(11)	(12)	(13)
20	13:30:5.896	47:13:16.646	0.508		0.027	0.010	55.393	1.267	0.039			
					2.926	0.868	639.684	129.887	0.351		0.098	
					0.010	0.004	41.428	0.452	0.062			
21	13:30:6.932	47:13:37.850	0.571		2.925	1.192	153.572	63.189	0.347		0.023	
					0.049	0.028	8.675	1.061	0.056			
22	13:29:44.689	47:12:28.622	0.298		2.962	1.155	720.355	93.450	0.540		0.111	
					0.056	0.026	32.720	1.779	0.047			
23	13:29:46.362	47:12:32.866	0.258	0.155	2.906	0.983	1004.989	98.683	0.244	8.606	0.152	8.869
				0.008	0.015	0.006	15.312	0.498	0.015	0.005		
24	13:29:47.560	47:12:35.887	0.233		2.903	0.704	638.925	68.805	0.230		0.097	7.079
					0.026	0.011	15.108	0.606	0.024			
25	13:29:49.347	47:12:40.432	0.206	0.001	2.986	1.080	6499.730	307.407	0.664		1.012	9.420
					0.028	0.010	279.806	2.867	0.042			
26	13:29:50.354	47:12:43.014	0.197	0.139	2.934	0.713	1322.978	94.027	0.392	8.585	0.202	9.105
				0.007	0.035	0.015	27.473	1.125	0.023	0.005		
27	13:29:51.083	47:12:44.854	0.194		2.965	1.023	1841.999	123.719	0.557		0.285	9.713
					0.026	0.011	45.989	1.068	0.025			
28	13:29:52.295	47:12:47.917	0.195	0.092	2.904	0.806	1350.585	177.085	0.236	8.636	0.205	8.667
				0.004	0.016	0.006	17.255	0.983	0.013	0.004		
29	13:29:45.026	47:13:30.791	0.412		2.977	1.189	3051.277	266.865	0.617		0.474	
					0.054	0.021	157.654	4.818	0.052			
30	13:29:47.109	47:13:40.363	0.399	0.453	2.889	1.067	690.511	76.383	0.154	8.514	0.104	6.521
				0.016	0.025	0.011	16.485	0.656	0.024	0.004		
31	13:29:50.629	47:09:23.297	0.419		2.983	1.020	1064.178	61.779	0.648		0.166	7.941
					0.027	0.013	42.680	0.551	0.039			
32	13:29:50.500	47:09:48.318	0.346		2.987	0.795	3885.289	306.589	0.669		0.605	
					0.032	0.009	148.490	3.306	0.038			
33	13:29:50.211	47:10:45.049	0.188		2.953	0.466	1136.890	67.431	0.491		0.175	9.460
					0.030	0.010	75.436	0.680	0.064			
34	13:29:44.762	47:09:59.469	0.398	0.110	2.936	0.910	3401.850	102.866	0.403	8.629	0.521	6.541
				0.006	0.013	0.005	41.733	0.468	0.012	0.005		
35	13:29:43.868	47:10:23.378	0.369	0.080	2.918	1.035	2115.448	206.212	0.307	8.672	0.322	6.406
				0.003	0.027	0.010	41.355	1.895	0.021	0.004		
36	13:29:42.858	47:10:50.267	0.354		2.934	0.799	664.662	52.532	0.394		0.102	7.867
					0.033	0.015	24.363	0.592	0.036			
37	13:29:41.993	47:11:13.421	0.359		2.971	0.925	1043.371	85.908	0.589		0.162	6.888
					0.031	0.013	33.942	0.904	0.032			
38	13:29:39.272	47:08:41.315	0.688	0.439	2.953	1.110	3466.517	487.261	0.492	8.519	0.534	
				0.013	0.031	0.010	161.828	5.145	0.045	0.005		

Table 2 continued

Table 2 (*continued*)

ID	R.A.	Decl.	R/R_{25}	[O III]	H α	[N II]	H β	EW(H α)	$E(B - V)$	12+log(O/H)	Σ_{SFR}	log (age)
(1)	(2)	(3)	(4)	(5)	(6)	(7)	(8)	(9)	(10)	(11)	(12)	(13)
39	13:29:37.156	47:09:45.832	0.609	0.164	2.967	1.250	2137.881	286.519	0.567	8.621	0.331	
				0.015	0.062	0.024	179.446	6.035	0.082	0.012		
40	13:29:43.876	47:10:23.982	0.367	0.072	2.924	0.988	2434.352	230.308	0.342	8.677	0.371	6.497
				0.002	0.021	0.008	35.717	1.639	0.015	0.003		
41	13:29:48.025	47:10:30.862	0.260		2.936	1.035	349.008	41.773	0.407		0.053	9.264
					0.026	0.015	21.298	0.365	0.058			
42	13:29:50.826	47:10:35.504	0.208		2.919	0.836	284.159	35.640	0.316		0.043	9.326
					0.021	0.013	14.807	0.259	0.050			
43	13:29:53.108	47:10:39.322	0.189		2.950	0.889	586.697	27.272	0.476		0.090	8.868
					0.011	0.008	17.782	0.101	0.029			
44	13:29:55.184	47:10:42.741	0.197		2.992	1.609	1053.441	33.853	0.697		0.164	9.387
					0.021	0.015	71.388	0.239	0.065			
45	13:29:56.781	47:10:45.406	0.218		3.008	0.924	2256.569	58.309	0.776		0.354	8.706
					0.011	0.006	57.247	0.208	0.024			
46	13:30:0.959	47:09:29.408	0.484	0.148	2.881	1.247	1630.106	279.099	0.112	8.632	0.245	8.529
				0.007	0.022	0.009	60.678	2.171	0.036	0.006		
47	13:30:2.091	47:09:46.368	0.467	0.186	2.914	1.092	1106.449	332.863	0.286	8.598	0.168	6.538
				0.004	0.017	0.006	24.232	1.894	0.022	0.003		
48	13:30:2.900	47:09:58.576	0.459	0.158	2.914	1.118	1573.680	244.229	0.289	8.616	0.239	6.306
				0.011	0.020	0.007	40.949	1.675	0.025	0.007		
49	13:30:4.585	47:10:23.804	0.457	0.443	2.979	1.165	2033.249	248.794	0.631	8.521	0.316	
				0.077	0.103	0.039	220.600	8.594	0.108	0.020		
50	13:30:0.959	47:09:29.408	0.484	0.140	2.761	1.268	1895.726	481.286		8.643	0.273	
				0.006	0.019	0.007	76.012	3.320	0.039	0.005		
51	13:30:1.956	47:09:44.390	0.468	0.185	2.907	1.225	1113.187	406.040	0.254	8.609	0.169	7.594
				0.003	0.024	0.009	29.632	3.375	0.026	0.003		
52	13:30:2.812	47:09:57.244	0.460	0.227	2.890	1.264	2136.803	292.724	0.162	8.594	0.322	6.823
				0.005	0.021	0.008	48.534	2.092	0.023	0.003		
53	13:30:5.116	47:10:31.796	0.460		2.923	1.322	692.242	256.869	0.338		0.106	
					0.078	0.035	71.218	6.887	0.101			
54	13:30:5.804	47:10:42.096	0.467		2.939	0.793	684.261	117.833	0.421		0.105	
					0.063	0.027	49.141	2.513	0.071			
55	13:30:3.475	47:09:37.840	0.516	0.408	2.917	1.188	750.475	184.806	0.303	8.533	0.114	
				0.018	0.027	0.011	19.527	1.680	0.026	0.005		
56	13:30:3.376	47:09:54.292	0.479	0.265	2.946	1.068	752.139	90.336	0.459	8.562	0.116	8.304
				0.016	0.029	0.013	26.724	0.875	0.035	0.007		
57	13:30:3.274	47:10:11.815	0.442		2.943	1.026	416.521	98.427	0.441		0.064	10.003
					0.034	0.014	40.861	1.141	0.094			
58	13:30:2.322	47:14:7.911	0.529	0.636	2.933	1.283	1304.002	145.787	0.389	8.498	0.200	

Table 2 *continued*

Table 2 (*continued*)

ID	R.A.	Decl.	R/R_{25}	[O III]	H α	[N II]	H β	EW(H α)	$E(B - V)$	12+log(O/H)	Σ_{SFR}	log (age)
(1)	(2)	(3)	(4)	(5)	(6)	(7)	(8)	(9)	(10)	(11)	(12)	(13)
				0.033	0.058	0.027	132.318	2.891	0.098	0.011		
59	13:29:52.936	47:11:30.079	0.038	0.226	3.031	0.938	3476.111	15.156	0.894	8.563	0.550	9.455
				0.019	0.020	0.016	197.418	0.101	0.054	0.010		
60 ^a	13:29:53.236	47:11:41.106	0.018	1.807	3.026	6.841	2585.291	5.713	0.868	8.554	0.408	9.676
				0.045	0.031	0.038	200.606	0.058	0.074	0.008		
61	13:29:53.569	47:11:53.274	0.042		2.988	1.185	1711.401	15.184	0.674		0.267	9.376
					0.015	0.011	87.832	0.076	0.049			
62	13:29:54.064	47:12:11.552	0.096		2.903	0.623	1312.535	81.076	0.229		0.199	9.870
					0.027	0.010	44.247	0.766	0.033			
63	13:29:54.675	47:12:34.019	0.165		2.965	0.598	1249.179	65.953	0.554		0.193	
					0.049	0.019	88.499	1.082	0.069			
64	13:30:6.746	47:11:23.171	0.463		2.880	1.024	1203.968	263.298	0.109		0.181	
					0.282	0.103	270.323	25.733	0.232			
65	13:30:6.987	47:11:35.297	0.467		2.897	0.932	1031.370	166.016	0.197		0.156	
					0.060	0.021	65.357	3.442	0.063			
66	13:30:8.492	47:12:50.718	0.549		2.940	0.862	1424.019	133.896	0.428		0.218	
					0.035	0.013	136.055	1.578	0.091			
67	13:29:58.802	47:09:12.242	0.493	0.261	2.958	1.125	1310.088	92.598	0.519	8.568	0.202	8.187
				0.012	0.022	0.010	56.322	0.702	0.041	0.006		
68	13:29:54.250	47:09:23.365	0.418	0.590	2.949	1.693	235.730	38.776	0.472	8.530	0.036	9.609
				0.045	0.041	0.026	15.722	0.534	0.065	0.009		
69	13:29:49.761	47:10:40.805	0.206		2.874	0.661	228.848	65.277	0.073		0.034	8.434
					0.025	0.010	9.173	0.566	0.039			
70	13:30:6.877	47:12:26.095	0.477	0.466	2.925	1.208	551.844	94.427	0.344	8.521	0.084	
				0.023	0.029	0.014	34.419	0.925	0.060	0.007		
71	13:30:5.002	47:13:8.036	0.470	0.373	2.923	1.420	453.477	65.801	0.337	8.558	0.069	
				0.017	0.012	0.007	21.479	0.268	0.045	0.006		
72	13:30:4.684	47:13:1.087	0.451		2.942	1.409	796.267	70.970	0.437		0.122	
					0.047	0.025	52.773	1.128	0.065			
73	13:30:1.959	47:13:22.798	0.420	0.665	2.915	1.294	449.785	58.531	0.292	8.495	0.068	9.072
				0.035	0.054	0.031	32.993	1.086	0.072	0.009		
74	13:30:0.355	47:13:35.584	0.414	0.263	2.927	1.163	872.811	57.987	0.359	8.571	0.133	8.307
				0.018	0.017	0.009	28.582	0.346	0.032	0.007		
75	13:29:58.678	47:13:48.932	0.420	0.142	2.896	1.170	1094.139	143.473	0.193	8.630	0.165	8.806
				0.008	0.022	0.009	28.989	1.099	0.026	0.006		
76	13:29:57.902	47:13:55.098	0.426	0.113	2.894	1.180	748.891	133.163	0.181	8.652	0.113	6.828
				0.008	0.034	0.015	24.864	1.574	0.033	0.007		
77	13:29:57.129	47:14:1.251	0.434	0.194	2.905	1.235	548.942	91.334	0.239	8.606	0.083	8.134
				0.011	0.037	0.018	23.734	1.170	0.043	0.007		

Table 2 *continued*

Table 2 (*continued*)

ID	R.A.	Decl.	R/R_{25}	[O III]	H α	[N II]	H β	EW(H α)	$E(B - V)$	12+log(O/H)	Σ_{SFR}	log (age)
(1)	(2)	(3)	(4)	(5)	(6)	(7)	(8)	(9)	(10)	(11)	(12)	(13)
78	13:29:56.356	47:14:7.444	0.445	0.223	2.897	1.219	492.534	113.638	0.199	8.592	0.074	
				0.019	0.039	0.018	34.399	1.538	0.068	0.011		
79	13:29:51.416	47:11:59.316	0.066		2.987	0.633	2510.877	43.190	0.671		0.391	8.381
					0.026	0.012	140.849	0.370	0.054			
80	13:29:55.312	47:11:41.285	0.085	0.126	2.939	0.638	1873.356	75.878	0.419	8.583	0.287	7.608
				0.006	0.013	0.005	29.717	0.325	0.016	0.005		
81	13:29:54.543	47:12:1.225	0.081		2.938	0.476	2294.173	85.862	0.417		0.352	6.636
					0.019	0.006	43.555	0.559	0.019			
82	13:29:54.012	47:12:14.944	0.104		2.892	0.506	1539.194	161.937	0.171		0.232	6.569
					0.017	0.004	22.943	0.937	0.015			
83	13:29:53.060	47:12:39.595	0.170		2.952	0.662	5821.643	322.414	0.489		0.896	
					0.035	0.009	174.125	3.783	0.031			
84	13:29:52.625	47:12:50.828	0.203	0.195	2.974	1.831	2741.855	127.118	0.602	8.640	0.425	6.690
				0.022	0.125	0.179	127.577	5.345	0.060	0.015		
85	13:29:59.370	47:10:43.181	0.283		2.881	0.827	199.402	40.761	0.114		0.030	
					0.085	0.042	17.899	1.196	0.090			
86	13:29:52.053	47:11:37.357	0.026	0.308	3.012	1.234	3654.845	16.098	0.797	8.560	0.574	9.347
				0.020	0.012	0.009	175.295	0.065	0.046	0.007		
87	13:29:49.087	47:11:59.316	0.129		2.994	0.828	3401.924	121.463	0.706		0.531	
					0.033	0.011	305.322	1.321	0.086			
88	13:29:58.275	47:14:8.694	0.467		2.906	0.974	1355.002	140.732	0.245		0.205	
					0.036	0.013	81.642	1.760	0.058			
89	13:29:55.726	47:14:1.251	0.422	0.188	2.928	1.080	2022.547	124.729	0.361	8.596	0.309	7.569
				0.012	0.031	0.013	58.822	1.317	0.029	0.007		
90	13:29:52.544	47:13:51.953	0.385		2.907	1.016	428.078	70.205	0.251		0.065	7.277
					0.026	0.012	18.402	0.624	0.042			
91	13:29:47.131	47:13:36.161	0.387	0.142	2.928	0.980	746.196	59.876	0.364	8.612	0.114	6.934
				0.011	0.022	0.011	22.033	0.447	0.029	0.008		
92	13:29:56.323	47:14:10.713	0.454	0.686	2.903	1.292	371.324	91.463	0.228	8.493	0.056	
				0.038	0.059	0.030	25.222	1.870	0.067	0.009		
93	13:29:55.437	47:14:8.488	0.441	0.424	2.904	1.348	288.190	79.253	0.236	8.542	0.044	
				0.030	0.040	0.020	22.310	1.082	0.075	0.010		
94	13:29:50.541	47:13:56.032	0.405	0.298	2.914	1.130	1018.263	148.560	0.287	8.557	0.155	
				0.016	0.038	0.015	46.249	1.938	0.045	0.007		
95	13:29:47.567	47:13:48.465	0.414	0.360	2.911	1.164	464.696	96.794	0.274	8.543	0.071	
				0.025	0.047	0.022	32.692	1.552	0.068	0.010		
96	13:29:46.252	47:13:45.156	0.425	0.394	2.865	1.082	754.867	237.374	0.026	8.529	0.113	
				0.012	0.039	0.014	25.828	3.249	0.035	0.005		
97 ^a	13:29:52.698	47:11:42.617	0.001	3.168	2.915	5.522	2728.201	8.477	0.294	8.485	0.415	9.129

Table 2 *continued*

Table 2 (*continued*)

ID	R.A.	Decl.	R/R_{25}	[O III]	H α	[N II]	H β	EW(H α)	$E(B - V)$	12+log(O/H)	Σ_{SFR}	log (age)
(1)	(2)	(3)	(4)	(5)	(6)	(7)	(8)	(9)	(10)	(11)	(12)	(13)
				0.030	0.013	0.015	95.252	0.037	0.033	0.003		
98	13:29:54.712	47:11:58.629	0.080		2.925	0.570	1961.074	85.061	0.348		0.299	8.409
					0.018	0.007	55.911	0.533	0.028			
99 ^a	13:29:52.698	47:11:42.617	0.001	4.702	3.063	6.917	19719.426	10.870	1.058	8.465	3.151	9.568
				0.061	0.016	0.020	1608.681	0.057	0.078	0.008		
100	13:30:4.464	47:12:17.279	0.395		2.943	0.015	258.615	21.566	0.439		0.040	8.327
					0.024		11.683	0.173	0.043			
101	13:30:7.379	47:11:29.255	0.481		2.914	1.010	141.177	24.420	0.288		0.021	6.681
					0.059	0.031	10.425	0.498	0.073			
102	13:30:8.280	47:12:49.963	0.542	0.321	2.928	1.257	214.433	26.029	0.362	8.560	0.033	6.833
				0.031	0.038	0.022	12.358	0.339	0.056	0.011		
103	13:30:1.117	47:11:39.335	0.274	0.068	2.983	0.776	2767.862	57.473	0.649	8.658	0.431	8.297
				0.005	0.015	0.005	40.883	0.283	0.015	0.007		
104	13:29:50.819	47:09:18.394	0.432	0.497	2.947	1.105	156.914	13.075	0.461	8.507	0.024	8.272
				0.043	0.035	0.024	9.190	0.156	0.057	0.010		
105	13:29:53.701	47:08:38.541	0.549	0.285	2.873	1.114	178.119	96.303	0.069	8.561	0.027	6.734
				0.024	0.064	0.025	12.114	2.160	0.068	0.010		
106	13:29:44.304	47:09:58.178	0.410	0.135	2.894	0.874	1015.928	109.280	0.181	8.608	0.153	7.208
				0.007	0.020	0.007	23.571	0.772	0.023	0.005		
107	13:29:49.885	47:11:43.551	0.092	0.150	3.012	0.638	1593.361	20.881	0.800	8.565	0.250	9.254
				0.017	0.016	0.008	71.903	0.114	0.043	0.011		
108	13:29:51.830	47:12:58.038	0.227	0.211	2.967	0.685	363.291	18.167	0.564	8.541	0.056	8.671
				0.019	0.023	0.012	13.992	0.138	0.037	0.009		
109	13:29:38.796	47:12:12.349	0.464		2.947	1.137	86.684	14.268	0.463		0.013	
					0.068	0.042	9.764	0.327	0.109			
110	13:29:46.681	47:12:32.509	0.249	0.118	2.948	0.830	729.011	38.824	0.465	8.614	0.112	8.443
				0.014	0.019	0.008	22.820	0.255	0.030	0.012		
111	13:30:1.260	47:13:41.159	0.445	0.507	2.929	1.429	209.164	19.784	0.369	8.530	0.032	6.781
				0.039	0.032	0.021	11.255	0.213	0.052	0.009		
112	13:30:2.161	47:12:56.994	0.376	0.252	2.924	1.093	502.357	30.281	0.340	8.569	0.077	8.681
				0.015	0.020	0.010	19.931	0.205	0.038	0.007		
113	13:30:6.731	47:14:20.010	0.648	0.326	2.934	0.846	191.527	11.331	0.394	8.522	0.029	6.995
				0.021	0.024	0.016	5.679	0.094	0.029	0.007		

NOTE—(1): object number. (2)-(3): equatorial coordinate (J2000). (4): scaled galactocentric distance, where R is the galactocentric distance and R_{25} is the apparent major isophotal radius. (5)-(7): relative fluxes of [O III] λ 5007, [N II] λ 6583 and H α that are normalized to the H β flux. (8): H β flux in unit of $10^{-17} \text{ erg s}^{-1} \text{ cm}^{-2}$. (9): equivalent width of H α line in \AA . (10): gas-phase reddening in mag. (11): metallicity in dex. (12): SFR density in $\text{M}_{\odot} \text{yr}^{-1} \text{kpc}^{-2}$. (13): logarithmic stellar age in year. Each row is followed by another row presenting the error.

^a AGN region.

REFERENCES

- Bacon, R., Copin, Y., Monnet, G., et al. 2001, *MNRAS*, 326, 23
- Baldwin, J. A., Phillips, M. M., & Terlevich, R. 1981, *PASP*, 93, 5
- Barrera-Ballesteros, J. K., Heckman, T. M., Zhu, G. B., et al. 2016, *MNRAS*, 463, 2513
- Belfiore, F., Maiolino, R., Tremonti, C., et al. 2017, *MNRAS*, 469, 151
- Berg, D. A., Skillman, E. D., Croxall, K. V., et al. 2015, *ApJ*, 806, 16
- Bertin, E., & Arnouts, S. 1996, *A&AS*, 117, 393
- Bresolin, F., Garnett, D. R., & Kennicutt, R. C., Jr. 2004, *ApJ*, 615, 228
- Bresolin, F. 2007, *ApJ*, 656, 186
- Bruzual, G., & Charlot, S. 2003, *MNRAS*, 344, 1000
- Bryant, J. J., Owers, M. S., Robotham, A. S. G., et al. 2015, *MNRAS*, 447, 2857
- Bundy, K., Bershad, M. A., Law, D. R., et al. 2015, *ApJ*, 798, 7
- Calzetti, D., Kennicutt, R. C., Jr., Bianchi, L., et al. 2005, *ApJ*, 633, 871
- Cano-Díaz, M., Ávila-Reese, V., Sánchez, S. F., et al. 2019, *MNRAS*, 488, 3929
- Cardelli, J. A., Clayton, G. C., & Mathis, J. S. 1989, *ApJ*, 345, 245
- Catalán-Torrecilla, C., Gil de Paz, A., Castillo-Morales, A., et al. 2015, *A&A*, 584, A87
- Chabrier, G. 2003, *PASP*, 115, 763
- Cid Fernandes, R., Mateus, A., Sodré, L., et al. 2005, *MNRAS*, 358, 363
- Colombo, D., Meidt, S. E., Schinnerer, E., et al. 2014, *ApJ*, 784, 4
- Corbin, T. E., Urban, S. E., & Warren, W. H. 1991, *Astrophysical Catalogue Reference Stars* (Corbin and Urban 1991). Documentation for the machine-readable version
- Croxall, K. V., Pogge, R. W., Berg, D. A., et al. 2015, *ApJ*, 808, 42.
- Croxall, K. V., Pogge, R. W., Berg, D. A., et al. 2016, *ApJ*, 830, 4
- de Vaucouleurs, G., de Vaucouleurs, A., Corwin, H. G., et al. 1995, *VizieR Online Data Catalog*, VII/155
- Dobbs, C. L., Theis, C., Pringle, J. E., & Bate, M. R. 2010, *MNRAS*, 403, 625
- Domínguez, A., Siana, B., Henry, A. L., et al. 2013, *ApJ*, 763, 145
- Fabricant, D., Fata, R., Roll, J., et al. 2005, *Publications of the Astronomical Society of the Pacific*, 117, 1411
- Fan, Z., Wang, H., Jiang, X., et al. 2016, *Publications of the Astronomical Society of the Pacific*, 128, 115005
- Fisher, D. B., & Drory, N. 2010, *ApJ*, 716, 942
- Galbany, L., Anderson, J. P., Rosales-Ortega, F. F., et al. 2016, *MNRAS*, 455, 4087
- García-Benito, R., González Delgado, R. M., Pérez, E., et al. 2019, *A&A*, 621, A120
- Goad, J. W., de Veny, J. B., & Goad, L. E. 1979, *ApJS*, 39, 439
- González Delgado, R. M., Cid Fernandes, R., Pérez, E., et al. 2016, *A&A*, 590, A44
- Grillmair, C. J., Faber, S. M., Lauer, T. R., et al. 1997, *AJ*, 113, 225
- Ho, I.-T., Kudritzki, R.-P., Kewley, L. J., et al. 2015, *MNRAS*, 448, 2030
- Hu, N., Wang, E., Lin, Z., et al. 2018, *ApJ*, 854, 68
- Kauffmann, G., Heckman, T. M., Tremonti, C., et al. 2003, *MNRAS*, 346, 1055
- Kennicutt, R. C. 1998, *ARA&A*, 36, 189
- Kewley, L. J., Dopita, M. A., Sutherland, R. S., et al. 2001, *ApJ*, 556, 121
- Kewley, L. J., & Dopita, M. A. 2002, *ApJS*, 142, 35
- Kewley, L. J., Rupke, D., Zahid, H. J., et al. 2010, *ApJL*, 721, L48
- Kobulnicky, H. A., Kennicutt, R. C., & Pizagno, J. L. 1999, *ApJ*, 514, 544
- Kong, X., Charlot, S., Brinchmann, J., et al. 2004, *MNRAS*, 349, 769
- Kong, X., Lin, L., Li, J.-r., et al. 2014, *Chinese Astronomy and Astrophysics*, 38, 427
- Kormendy, J., & Kennicutt, R. C., Jr. 2004, *ARA&A*, 42, 603
- Lacerda, E. A. D., Cid Fernandes, R., Couto, G. S., et al. 2018, *MNRAS*, 474, 3727
- Lamers, H. J. G. L. M., Panagia, N., Scuderi, S., et al. 2002, *ApJ*, 566, 818
- Lin, L., Zou, H., Kong, X., et al. 2013, *ApJ*, 769, 127
- Lin, Z., Hu, N., Kong, X., et al. 2017, *ApJ*, 842, 97
- López-Sánchez, Á. R. 2010, *A&A*, 521, A63
- Marino, R. A., Rosales-Ortega, F. F., Sánchez, S. F., et al. 2013, *A&A*, 559, A114
- Mentuch Cooper, E., Wilson, C. D., Foyle, K., et al. 2012, *ApJ*, 755, 165
- Moustakas, J., Kennicutt, R. C., Jr., Tremonti, C. A., et al. 2010, *ApJS*, 190, 233
- Oey, M. S., & Kennicutt, R. C. 1993, *ApJ*, 411, 137
- Osterbrock, D. E., & Ferland, G. J. 2006, *Astrophysics of gaseous nebulae and active galactic nuclei*, 2nd edn. University Science Books, Mill Valley, CA

- Pettini, M., & Pagel, B. E. J. 2004, MNRAS, 348, L59
- Pilyugin, L. S., Vílchez, J. M., & Contini, T. 2004, A&A, 425, 849
- Pilyugin, L. S., & Thuan, T. X. 2005, ApJ, 631, 231
- Pilyugin, L. S., Grebel, E. K., & Kniazev, A. Y. 2014, AJ, 147, 131
- Rosales-Ortega, F. F., Sánchez, S. F., Iglesias-Páramo, J., et al. 2012, ApJL, 756, L31
- Salo, H., & Laurikainen, E. 2000, MNRAS, 319, 393
- Sánchez-Blázquez, P., Rosales-Ortega, F. F., Méndez-Abreu, J., et al. 2014, A&A, 570, A6
- Sánchez, S. F., Kennicutt, R. C., Gil de Paz, A., et al. 2012, A&A, 538, A8
- Sánchez, S. F., Rosales-Ortega, F. F., Iglesias-Páramo, J., et al. 2014, A&A, 563, A49
- Sánchez, S. F., Pérez, E., Rosales-Ortega, F. F., et al. 2015, A&A, 574, A47
- Sánchez, S. F. 2020, ARA&A, 58, annurev
- Sánchez-Menguiano, L., Sánchez, S. F., Pérez, I., et al. 2018, A&A, 609, A119
- Sánchez-Menguiano, L., Sánchez Almeida, J., Muñoz-Tuñón, C., et al. 2019, ApJ, 882, 9
- Schlegel, D. J., Finkbeiner, D. P., & Davis, M. 1998, ApJ, 500, 525
- Searle, L. 1971, ApJ, 168, 327
- Skrutskie, M. F., Cutri, R. M., Stiening, R., et al. 2006, AJ, 131, 1163
- Spillar, E. J., Oh, S. P., Johnson, P. E., & Wenz, M. 1992, AJ, 103, 793
- Tremonti, C. A., Heckman, T. M., Kauffmann, G., et al. 2004, ApJ, 613, 898
- Walter, F., Brinks, E., de Blok, W. J. G., et al. 2008, AJ, 136, 2563
- Zahid, H. J., Dima, G. I., Kudritzki, R.-P., et al. 2014, ApJ, 791, 130
- Zaritsky, D., Kennicutt, R. C., & Huchra, J. P. 1994, ApJ, 420, 87
- Zhou, Z., Wu, H., Huang, L., Li, H., Zhou, Z., Jia, J., Lam, M., & Zhu, Y. 2014, Research in Astronomy and Astrophysics (RAA), 14, 11, 1393
- Zinchenko, I. A., Just, A., Pilyugin, L. S., et al. 2019, A&A, 623, A7
- Zou, H. 2011, PASP, 123, 1135
- Zou, H., Yang, Y.-B., Zhang, T.-M., et al. 2011, Research in Astronomy and Astrophysics, 11, 1093
- Zou, H., Zhang, W., Yang, Y., et al. 2011, AJ, 142, 16